



# Structural characteristics of irrational Type-II Twin interfaces

Ahmed Sameer Khan Mohammed, Huseyin Sehitoglu\*

Department of Mechanical Science and Engineering, University of Illinois at Urbana-Champaign, 1206W Green St, Urbana, IL 61801, USA

## ARTICLE INFO

### Keywords:

Twin boundary  
Type II twin  
Functional materials  
Interface  
Topology

## ABSTRACT

The Type-II Twin Boundary (TB) is a critical interface in functional materials whose irrational Miller-index identity has recently drawn significant research interest. This study establishes general structural characteristics of the Type-II twin interface, utilizing TBs in Shape Memory Alloys (SMAs) - TiPd, TiPt, and AuCd - as study targets. It is shown how the irrational identity of each TB is explained by the Terrace-Disconnection (T-D) structural topology. It is proposed that the terrace is the rational-plane nearest to the irrational TB in the reciprocal space, having integral Miller-indices of least magnitude. Crystallographic-registry on this terrace requires non-trivial coherence-strains. A novel kinematic-origin of the coherence-strain is proposed, coming directly from a transformation of the classical twinning deformation-gradient. This transformation revealed that the classical twinning-shear partitions into the coherence-strain and a new metric termed the “terrace-shear”. It is shown that the magnitude of shear relating the twin-structure to the matrix is the terrace-shear and not the twinning-shear, contrary to classical understanding. Furthermore, the Burgers vector of the twinning disconnection is shown to be related directly to the terrace-shear. The energy of each Type-II interface is determined from ab initio Density Functional Theory (DFT) calculations. It is shown that the energy-minimal atomic-structure on the terrace requires determination of a “lattice-offset” that is non-trivial and unknown apriori. In summary, this study expounds on T-D topological structure of Type-II twin interfaces, establishing methods to identify rational terraces, coherence strains, ab initio planar TB energies and revealing a unique partitioning of the twinning-shear exhibited by this class of interfaces.

## 1. Introduction

Twin Boundaries (TBs) are ubiquitous interfaces prominent in multiple materials spanning structural, functional, semiconductor, and two-dimensional materials (Gengor et al., 2021; Jozaghi et al., 2022; Rooney et al., 2018; Rothmann et al., 2017; Wang et al., 2015; Zárubová et al., 2010). In these materials, TBs critically influence properties such as material strength (Lu, 2016; Zhang et al., 2017; Zhao et al., 2021), strain-hardening capacity (Bönisch et al., 2018a; Bönisch et al., 2018b; Celebi et al., 2022; Chowdhury et al., 2016b), fatigue-resistance (Alkan et al., 2016; Chowdhury et al., 2016a, 2016b), functional/actuating characteristics (Bucsek et al., 2019; Mohammed and Sehitoglu, 2020a; Müllner et al., 2003; Sidharth et al., 2021; Šittner et al., 2020) and electron-transport properties (Blömers et al., 2011; Qian et al., 2015). In addition to their technological relevance, TB structures are scientifically instructive as they portray versatile behaviors across the spectrum of interface-coherency (from fully-coherent, to semi-coherent and also incoherent) and serve as benchmarks to understand grain boundaries and other crystalline interfaces in general (Beyerlein et al.,

\* Corresponding author.

E-mail address: [huseyin@illinois.edu](mailto:huseyin@illinois.edu) (H. Sehitoglu).

**Table 1**

Crystallography of Type II TBs in SMAs considered in this study (the indices of  $K_1$  are calculated following the procedure outlined in [Appendix A](#)).

| Material | Austenitic crystal structure   | Martensitic crystal structure  | Lattice-Motif atomic positions   | Crystallography of Type II Twin Boundary                               |
|----------|--|--|--|--|
| TiPd     | B2 cubic<br>$a_0 = 3.18 \text{ \AA}$<br>(Donkersloot and Van Vucht, 1970)  | B19 Orthorhombic<br>$a = 4.89 \text{ \AA}$ , $b = 2.81 \text{ \AA}$ ,<br>$c = 4.56 \text{ \AA}$<br>(Dwight et al., 1965) | Ti (0, 0, 0), (0.402, 0, 0.5)<br>Pd (0.89, 0.5, 0.5), (0.512, 0.5, 0)<br>(Ye et al., 1997)     | $K_1 = (\bar{1} \ 0.678 \ \bar{0}.356)$<br>$\eta_1 = [121], s = 0.361$ |
| TiPt     | B2 cubic<br>$a_0 = 3.192 \text{ \AA}$<br>(Donkersloot and Van Vucht, 1970) | B19 Orthorhombic<br>$a = 4.84 \text{ \AA}$ , $b = 2.76 \text{ \AA}$ ,<br>$c = 4.59 \text{ \AA}$<br>(Dwight et al., 1965) | Ti (0, 0, 0), (0.394, 0, 0.5)<br>Pt (0.885, 0.5, 0.5), (0.509, 0.5, 0)<br>(Ye et al., 1997)    | $K_1 = (\bar{1} \ 0.748 \ \bar{0}.497)$<br>$\eta_1 = [121], s = 0.386$ |
| AuCd     | B2 cubic<br>$a_0 = 3.323 \text{ \AA}$<br>(Morii et al., 1991)              | B19 Orthorhombic<br>$a = 4.86 \text{ \AA}$ , $b = 3.15 \text{ \AA}$ ,<br>$c = 4.766 \text{ \AA}$<br>(Ohba et al., 1990)  | Cd (0, 0, 0), (0.41, 0, 0.5)<br>Au (0.9053, 0.5, 0.5), (0.5047, 0.5, 0)<br>(Ohba et al., 1990) | $K_1 = (\bar{1} \ 0.786 \ \bar{0}.572)$<br>$\eta_1 = [121], s = 0.156$ |

2014; Mohammed and Sehitoglu, 2020b; Zhu et al., 2022). Therefore, it is vital to develop a thorough understanding of the structure and energies of twin interfaces.

This study focuses on TBs in the class of functional materials known as Shape Memory Alloys (SMAs), where twinning is widely prevalent as a mode of Lattice-Invariant-Deformation (LID) accompanying phase-transformation mechanisms in the material. A prevalent twinning mode in these materials is the Type-II twin mode (Adachi et al., 1986; Hara et al., 1992; Knowles, 1982; Liu and Dunne, 2003; Morii et al., 1991; Nishida et al., 1997, 2008b; Okamoto et al., 1986; Xie and Liu, 2004; Zou et al., 2018) where the type-classification comes from the relation between the lattice-orientations of the twin variants. Three major orientation relationships were defined by the classical theory of deformation twinning (Bilby and Crocker, 1965; Christian and Mahajan, 1995), presented here in brief for the reader's convenience:

- I. Type I twins: The lattices of the twin variants are related by mirror symmetry with the TB being the mirror plane
- II. Type II twins: The lattices of the twin variants are related by a  $180^\circ$  rotational symmetry about an axis along the direction of twinning shear
- III. Compound twins: The lattices of the twin variants obey both symmetries defining Type-I and Type-II twins.

The nature of symmetry obeyed by the twin-variants in Type-I and Compound twinning modes allow their TBs to exhibit rational Miller-index identities, defining an unambiguous crystallographic plane for the TB. Type-II TBs, on the other hand, uniquely distinguish themselves by exhibiting irrational Miller indices. Their underlying structure is consequently more complex and has been a topic of recent research interest (Hirth and Wang, 2021; Karki et al., 2020; Mohammed and Sehitoglu, 2020b, 2021; Müllner, 2019; Pond and Hirth, 2018; Pond et al., 2019).

The presence and mobility of Type-II twins has important implications to mechanical behavior of SMAs. Fatigue in SMAs is governed by cyclic accumulation of transformation-induced plastic strains, known to be caused by the emission of slip-dislocations from internal martensitic TBs (Kajiwar and Kikuchi, 1982; Kajiwar and Owen, 1973; Mohammed and Sehitoglu, 2020a; Norfleet et al., 2009; Simon et al., 2010). The equilibrium TB energy dictates the twin density accompanying the martensitic transformation, consequently impacting the propensity for transformation-induced plasticity and fatigue. The mobility of the TB influences the ease of TB migration and detwinning, impacting the functional performance of ferromagnetic SMAs such as NiMnGa (Heczko, 2014; Zou et al., 2018). The role of TB disconnections in dictating twinning mechanisms and TB mobility has also drawn significant research attention, especially in recent times (Gong et al., 2021, 2022; Hirth et al., 2020; Li et al., 2023; Wang et al., 2024; Xu et al., 2022). Therefore, a clear understanding of the structure, topology, and energy of Type II TBs is a necessary precursor to assess their influence on mechanical behavior of SMAs.

The Terrace-Disconnection (T-D) topology has been recently proposed as an energetically-favorable structural model for the irrationality of the Type II TB, reconciling with experimental results and the topologies of TBs of other types (Type I and Compound) (Mohammed and Sehitoglu, 2021). Briefly, the T-D topology explains the irrationality as an array of periodically spaced twinning disconnections residing on a rational terrace plane, such that the effective stepped-structure exhibits an irrational identity. Previously, significant focus has been attributed to the NiTi system, where the scientific and commercial success of the material's functionality fostered strong prior research on experimental and modeling fronts directed toward understanding its Type-II TB (Ezaz and Sehitoglu, 2011; Knowles, 1982; Knowles and Smith, 1981; Liu and Xie, 2003; Mohammed and Sehitoglu, 2020b; Nishida et al., 2008a, 1995a; Pond et al., 2019; Xie and Liu, 2004). This study examines the applicability of the Terrace-Disconnection (T-D) topology to explain irrationality of the Type II TBs in other SMAs (namely TiPd, TiPt and AuCd) and determine the energies of the interface. By doing so, the goal is to develop a general framework to model Type II TBs in general and to reveal novel characteristics of the irrational TB that have broader relevance beyond a given specific alloy system. Experimental evidence of Type II TBs in the selected SMAs can be found in refs. (Morii et al., 1991; Nishida et al., 1997, 2008b), for instance.

Table 1 lists all the lattice parameters, atomic positions, and crystallography of the twin interfaces considered in this study. The 3 SMAs considered exhibit a B2 austenitic phase and transform to a B19-orthorhombic martensitic phase. The B19 phase has been proposed to be similar to the Hexagonal Close-Packed (HCP) phase, based on parallels drawn between the B2-to-B19 transformation

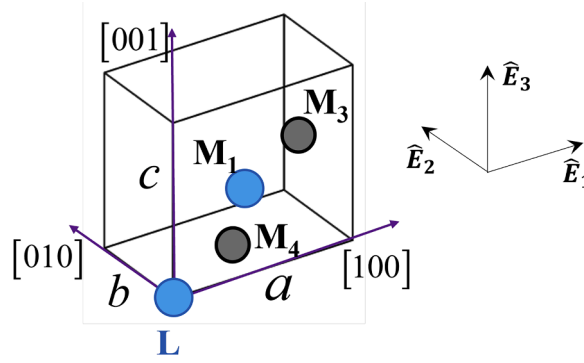


**Fig. 1.** B19 Orthorhombic unit cell of martensitic crystal structures of SMAs considered in this study, comprising unequal lattice parameters  $a$ ,  $b$ , and  $c$ , and atomic-sites at lattice (L) and Motif (M) positions; All SMAs in this study have two elemental species, one of them is indicated in blue and the other in gray; an orthonormal coordinate system  $\hat{E}_1 - \hat{E}_2 - \hat{E}_3$  aligned with the crystallographic lattice vectors is also shown.

and Body-Centered-Cubic (BCC)-to-HCP transformation mechanisms (Huang et al., 2003). A theoretical analysis of the cubic-to-orthorhombic phase-change based on the phenomenological theory of martensitic transformation can be found in ref. (Lieberman et al., 1955). Martensitic phases generally exhibit high yield stresses for slip (Sehitoglu et al., 2000) in SMAs and deform through internal detwinning or TB migration. Three evident twinning modes in the B19 phase is the  $\{111\}$  Type I twin mode,  $\{101\}$  Compound twin mode and the  $\langle 121 \rangle$  Type II twin mode (Mori et al., 1991; Nishida et al., 2008b), the last of which is the twinning mode of focus in this study.

It is worth emphasizing that the Type II twin mode considered in this study is the conjugate to the  $\{111\}$  Type I twin mode in all the B19-orthorhombic systems. The Type II TBs are observed in the B19 phase, a generalized unit cell description of which is provided in Fig. 1. The atomic-site at the lattice point of the unit cell is termed a lattice-site and the remaining atomic-positions within the cell are defined as the motif points. To begin with, there is no basis for the choice of rational terrace preferred by the TBs in these materials. This issue is very much unlike NiTi where significant prior research work identified the  $(11\bar{1})$  plane as the rational terrace for the irrational  $K_1 = (0.7205 \ 1 \ \bar{1})$  TB (Knowles, 1982; Knowles and Smith, 1981; Liu and Xie, 2003, 2006; Nishida et al., 2008a, 1995a, 1995b; Xie and Liu, 2004). Thus, an evaluation of the newer Type-II systems listed in Table 1 offers the opportunity to examine the basis behind determination of the rational terrace. Once this terrace is identified, the atomistic structure needs to be determined in order to compute the TB energy. Here again, there is no benefit of a reliable interatomic potential as is available in the case of NiTi (Kim et al., 2017; Ko et al., 2015; Muralles et al., 2017; Ren and Sehitoglu, 2016; Zhong et al., 2011). To determine the atomic-structure on the terrace, a key unknown to be computed is known as the “lattice-offset” which specifies the relative positioning of the twin lattice with respect to the matrix. Given the challenge of absence of reliable potentials, it provides the opportunity to determine lattice-offsets more accurately using Density Functional Theory (DFT) calculations as proposed in this study. Furthermore, the analysis of the new Type-II systems reveals an important distinction between the classical twinning shear and the “terrace-shear” carried by the twinning disconnections on rational terraces, revealed for the first time in this study to the best of the authors’ knowledge. The simulation methods and results of the study are elaborated in Section 2, implications of these results are discussed in Section 3, and the conclusions of the study are presented in Section 4.

## 2. Methodology and results

This section describes the methodology for defining the T-D topology and the determination of the atomic-structure on the terraces, presenting the results concurrently. First in Section 2.1, a formal framework to determine the rational terraces is provided. In Section 2.2, The presence of coherence-strains on the terraces is illustrated from a crystallographic standpoint following which a continuum origin for these strains is revealed, obtained directly from the twinning deformation-gradient. Next, a distinction between the classical twinning shear and a newly-defined “terrace-shear” is forwarded in Section 2.3, noting the stronger physical relevance of the latter metric over the former classical definition. Subsequently, the Burgers vector of the twinning disconnection is calculated in Section 2.4 and it is shown that its magnitude relates to the terrace-shear and not the twinning shear. The periodic spacing between the array of disconnections in the T-D topology is calculated using the Frank-Bilby equation and the resulting structure is shown to explain the irrational Miller indices of each Type II TB. Finally in Section 2.5, the energy of the TB is calculated from ab initio DFT simulations. The lattice-parameters and lattice-motif atomic positions suited to the chosen pseudopotentials are determined. The atomic-structure on the rational terraces is established by defining and calculating the lattice-offset on the terrace. The equilibrium TB energy is then determined at the value of lattice-offset that yields the lowest energy.

### 2.1. Rational terrace for the Type II TB

The rational-terrace with the least Miller-indices is determined for each of the irrational TBs listed in Table 1. For this purpose, the real-space and reciprocal-space lattices of the martensitic crystal structure must be defined. The real-space lattice can be defined by a

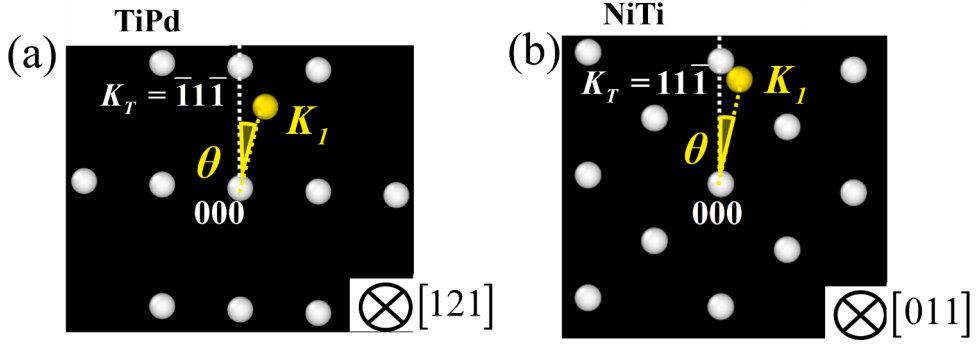


**Fig. 2.** Identification of nearest “least-index” rational terrace of Type II TB from the reciprocal space of the underlying lattice, shown for (a) TiPd, where  $K_I = (\bar{1} \ 0.678 \ 0.356)$ ,  $\theta = 17.22^\circ$  and the rational terrace is  $K_T = (\bar{1}1\bar{1})$ , and for the better known case of (b) NiTi, where  $K_I = (0.7205 \ 1 \ \bar{1})$ ,  $\theta = 10.07^\circ$  and the rational terrace is  $K_T = (11\bar{1})$ .

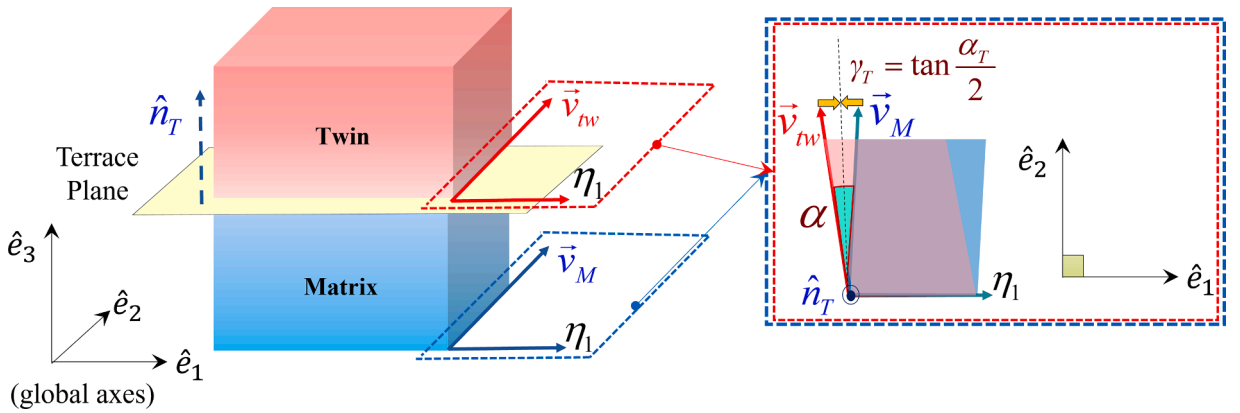


**Fig. 3.** Crystallography of the rational terrace plane with normal  $\hat{n}_T$ , indicating the common twinning direction  $\eta_1$ , shear-mismatch between lattice vectors  $\vec{v}_{tw}$  and  $\vec{v}_M$  and coherence strain  $\gamma_T$  required for atomic-registry on the rational terrace; the orthonormal global axes  $\hat{e}_1 - \hat{e}_2 - \hat{e}_3$  are also indicated.

matrix  $C_{LAT}$  in which the columns represent the components of the crystallographic basis  $[100] - [010] - [001]$  in reference to an orthonormal coordinate system  $\hat{E}_1 - \hat{E}_2 - \hat{E}_3$  (shown in Fig. 1), given by the equation:

$$C_{LAT} = \begin{pmatrix} a & 0 & 0 \\ 0 & b & 0 \\ 0 & 0 & c \end{pmatrix} \quad (1)$$

where  $a$ ,  $b$  and  $c$  are the lattice constants of the orthorhombic B19 phase. The components of any crystallographic lattice vector  $[uvw]$  is then given by  $C_{LAT} \begin{pmatrix} u \\ v \\ w \end{pmatrix}$ . The reciprocal space lattice is then defined by the matrix  $P_{LAT}$ :

$$P_{LAT} = (C_{LAT})^{-T} \quad (2)$$

where the columns of  $P_{LAT}$  represent the components of the unit-cell lattice vectors of the reciprocal lattice and the superscript  $(-T)$  refers to the inverse-of-transpose (or equivalently the transpose-of-inverse) matrix operation. The components of the normal of any crystallographic plane is given by  $\hat{n} = d_{(hkl)} P_{LAT} \begin{pmatrix} h \\ k \\ l \end{pmatrix}$ , where  $d_{(hkl)}$  is the interplanar spacing given by the inverse-norm of  $P_{LAT} \begin{pmatrix} h \\ k \\ l \end{pmatrix}$ .

With the reciprocal lattice defined, all crystallographic planes  $(hkl)$  are plotted in this space and the irrational TB  $K_I$  is also plotted. By viewing the reciprocal space along the direction of twinning  $\eta_1 = [121]$ , the crystallographic plane nearest to  $K_I$  is proposed to be the rational terrace  $K_T$ , illustrated in Fig. 2. More precisely, the rational terrace is one which has the nearest normal to that of the irrational interface  $K_I$ . The angle of inclination  $\theta$  between the normal to the terrace plane  $K_T$ , say with indices  $(h_T k_T l_T)$  and interplanar spacing  $d_{(h_T k_T l_T)}$ , and the normal to the irrational TB plane  $K_I$ , with indices  $(hkl)$  and interplanar spacing  $d_{(hkl)}$ , is calculated following the

**Table 2**

Coherence-strains required on rational terraces of Type II TBs.

| Material | Type II Twin Boundary ( $\mathbf{K}_1$ ) | Twinning shear, $s$ | Rational-Terrace $\mathbf{K}_T$ (with normal $\hat{\mathbf{n}}_T$ ) | Coherence-strain, $\gamma_T$ (%) | Terrace-Shear, $s_T$ |
|----------|--|---------------------|---|----------------------------------|----------------------|
| TiPd     | $(\bar{1} \ 0.678 \ 0.356)$              | 0.361               | $(\bar{1}1\bar{1})$   | 5.35                             | 0.345                |
| TiPt     | $(\bar{1} \ 0.748 \ 0.497)$              | 0.386               | $(\bar{1}1\bar{1})$   | 4.09                             | 0.376                |
| AuCd     | $(\bar{1} \ 0.786 \ 0.572)$              | 0.156               | $(\bar{1}1\bar{1})$   | 1.42                             | 0.153                |

equation:

$$\theta = \cos^{-1}(\hat{\mathbf{n}}_K \cdot \hat{\mathbf{n}}_T) \quad (3)$$

where  $\hat{\mathbf{n}}_K = d_{(hkl)} P_{LAT} \begin{pmatrix} h \\ k \\ l \end{pmatrix}$  and  $\hat{\mathbf{n}}_T = d_{(h_T k_T l_T)} P_{LAT} \begin{pmatrix} h_T \\ k_T \\ l_T \end{pmatrix}$ . Note that the direction of twinning has orthonormal components given by  $C_{LAT} \eta_1$  and the reciprocal lattice is viewed along this vector. The rational terrace for all the B19 orthorhombic systems in Table 1 is found to be  $\mathbf{K}_T = (\bar{1}1\bar{1})$ . The case of NiTi is also illustrated for reference where the rational terrace  $\mathbf{K}_T = (11\bar{1})$  is well-known for the irrational type II TB.

## 2.2. Coherence strains on the rational terrace $\mathbf{K}_T$

Having established the rational-terrace, the crystallography on the terrace must be examined to construct the equilibrium atomic-structure on this plane. The crystallography is defined with reference to a new orthonormal coordinate system  $\hat{\mathbf{e}}_1 - \hat{\mathbf{e}}_2 - \hat{\mathbf{e}}_3$  (refer Fig. 3). The lattice of the matrix variant is defined as follows. The direction of twinning  $\eta_1 = [121]$  is aligned with  $\hat{\mathbf{e}}_1$ , the normal to the rational terrace  $\mathbf{K}_T = (\bar{1}1\bar{1})$ , given by  $\hat{\mathbf{n}}_T$ , is aligned parallel to  $\hat{\mathbf{e}}_3$ . The  $C_{LAT}^M$  matrix, introduced in Section 2.1, can be redefined consistent with this orientation for the matrix variant, and for the case of TiPd, is given by:

$$C_{LAT}^M = \begin{pmatrix} 2.7377 & 1.8080 & 2.3807 \\ 3.4350 & -0.0967 & -3.2417 \\ -2.1489 & 2.1489 & -2.1489 \end{pmatrix} \quad (4)$$

The crystallography of the twin variant is chosen consistent with the Type II orientation relationship, where the twin is related to the matrix by a  $180^\circ$  rotation about the direction of twinning (Bilby and Crocker, 1965). Consequently, for the twin variant,  $C_{LAT}^{tw}$  is given by:

$$C_{LAT}^{tw} = (2(\hat{\eta}_1 \otimes \hat{\eta}_1) - I) C_{LAT}^M \quad (5)$$

where  $\hat{\eta}_1 = C_{LAT}^M \eta_1 / |C_{LAT}^M \eta_1|$  is the unit vector along the direction of twinning  $\eta_1 = [121]$ . Having defined these orientations, the crystallographic registry between the twin variants on the rational terrace must be addressed. There exists a shear-mismatch on the rational-terrace  $\mathbf{K}_T$  as illustrated in Fig. 3. With the twinning direction  $\eta_1$  aligned in both variants, the vectors  $\vec{\mathbf{v}}_M = [10\bar{1}]_M$  and  $\vec{\mathbf{v}}_{tw} = [\bar{1}01]_{tw}$  are misaligned. An in-plane shear-strain,  $\gamma_T$  must be applied to both the twin and matrix variants for atomic-registry on the terrace (Fig. 3). The magnitude of the shear-strains for all SMAs considered is listed in Table 2, and note that the magnitudes are significant, of the order of few percent. The coherently-strained lattices are defined by the matrices in Eq. (6).

$$C_{LAT}^{M,C} = \begin{pmatrix} 1 & -\gamma_T & 0 \\ 0 & 1 & 0 \\ 0 & 0 & 1 \end{pmatrix} C_{LAT}^M \quad (6)$$

$$C_{LAT}^{tw,C} = \begin{pmatrix} 1 & \gamma_T & 0 \\ 0 & 1 & 0 \\ 0 & 0 & 1 \end{pmatrix} C_{LAT}^{tw}$$

## 2.3. Concept of ‘‘Terrace-shear’’ and distinction from classical twinning shear

Thus far, the necessity of a coherence-strain was determined from crystallographic considerations on the rational terrace plane. In this section, a physical origin from a continuum mechanics standpoint is offered, noted for the first time in literature, to the best of the authors’ knowledge. From classical twinning theory (Bilby and Crocker, 1965) and conventional understanding of twinning, it is well established that the twin variant is related to the matrix by an Invariant Plane Strain (IPS) and the invariant plane is the plane of twinning. The IPS is given by the deformation gradient of the form:

$$F_{tw} = (I + s(\hat{\eta}_1 \otimes \hat{\mathbf{n}}_K)) \quad (7)$$

where  $s$  is the classical twinning shear (listed in Table 1), the unit vector along the direction of twinning  $\hat{\eta}_1$  and the unit normal  $\hat{\mathbf{n}}_K$  of

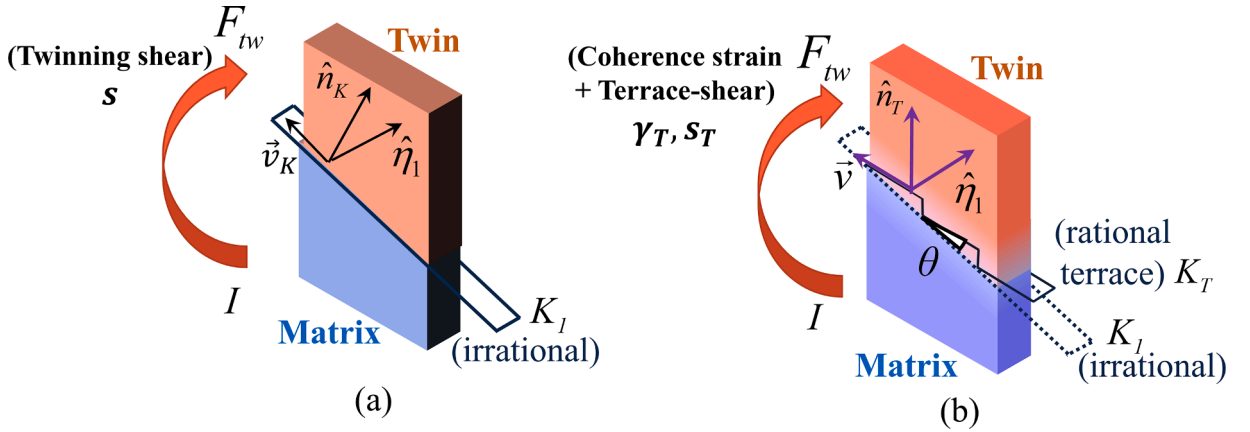


**Fig. 4.** Deformation gradient relating the twin to the matrix described in two frames of reference (a) the conventional coordinate system based on normal to the irrational plane of twinning  $\hat{n}_K$ , direction of twinning shear  $\eta_1$  and a third orthonormal vector  $\vec{v}_K$ ; the deformation-gradient only reveals the classical twinning shear  $s$  in this system. (b) In the terrace coordinate system described by the terrace-normal  $\hat{n}_T$ , twinning-shear direction  $\eta_1$  and third orthonormal vector  $\vec{v}$ , the deformation-gradient reveals both the coherence-strain  $\gamma_T$  and the terrace-shear  $s_T$ ; the angle between the rational terrace and irrational plane,  $\theta$ , is also illustrated.

the irrational twinning plane (refer figure 4(a)). In the coordinate system  $\hat{\eta}_1 - \vec{v}_K - \hat{n}_K$  defined on the irrational twinning plane, the deformation gradient is given by:

$$[F_{tw}]_K = \begin{pmatrix} 1 & 0 & s \\ 0 & 1 & 0 \\ 0 & 0 & 1 \end{pmatrix} \quad (8)$$

Consider the same deformation gradient resolved along a coordinate system attached to the rational terrace plane,  $\hat{\eta}_1 - \vec{v} - \hat{n}_T$  as illustrated in figure 4(b). In this coordinate system, the deformation gradient is obtained from a rotational transformation, given by the following equations:

$$[F_{tw}]_T = [Q]^T [F_{tw}]_K [Q]$$

$$[Q] = \begin{pmatrix} 1 & 0 & 0 \\ 0 & \cos\theta & \sin\theta \\ 0 & -\sin\theta & \cos\theta \end{pmatrix} \quad (9)$$

$$[F_{tw}]_T = \begin{pmatrix} 1 & -\gamma_T & s_T \\ 0 & 1 & 0 \\ 0 & 0 & 1 \end{pmatrix}$$

where  $\theta$  is the angle between the irrational plane  $K_I$  and the rational terrace  $K_T$  (refer Figs. 4 and 2, illustrating the angle in real and reciprocal spaces respectively). Note that the components of the deformation gradient  $F_{tw}$  resolved in the terrace coordinate system (described by  $[F_{tw}]_T$  in Eq. (9)) directly yields the coherence strain  $\gamma_T$ . Additionally, a new metric  $s_T$  is revealed which is defined as the “terrace-shear”. The terrace-shear  $s_T$  is the shear required to twin on the rational terrace. It transforms the coherently-strained matrix to the coherently-strained twin variant, and recall that these coherence-strains are necessary for atomic-registry on the terrace. From Eqs. (8) and (9), the terrace-shear,  $s_T$ , and coherence-strain,  $\gamma_T$ , can be determined as functions of  $\theta$  and  $s$  as follows:

$$s_T = s \cos\theta; \gamma_T = s \sin\theta \quad (10)$$

Figure 5(a) illustrates the role of terrace-shear  $s_T$  in twinning the atomic-structure on the terrace-plane for TiPd. A comparison is provided with the well-studied  $\{111\}$  twinning mode in Face-Centered-Cubic materials (Copper, Cu, chosen as example) shown in figure 5(b), where such a distinction between terrace-shear and twinning-shear is not required. The significance of this distinction will be discussed in Section 3. Table 2 lists all the terrace-shears for the SMA systems considered, note that they are all not equal to the respective classical twinning shears. The following section outlines another physical significance of the terrace-shear in how it connects with the Burgers vector of the twinning disconnection.

#### 2.4. Twinning disconnection Burgers vector and Terrace-Disconnection topology of Type II TBs

Defining the Terrace-Disconnection (T-D) topology requires the Burgers vector and step height of the twinning disconnection. The Burgers vector is determined following the methods developed in refs. (Bilby and Crocker, 1965; Hirth and Pond, 1996; Karki et al.,

**Table 3**

Effective irrational-plane predicted by Terrace-Disconnection topology, through the Frank-Bilby equation.

| Material | Burgers vector of twinning disconnection $ \vec{b}_{TW} $ (Å) | Spacing between disconnections, $d$ (Å) | Angle of deviation, $\theta$ | Type II Twin Boundary ( $K_1$ ) |
|----------|---|---|------------------------------|---------------------------------|
| TiPd     | 1.482   | 13.85                                   | 17.24                        | ( $\bar{1}$ 0.678 0.355)        |
| TiPt     | 1.608   | 12.2                                    | 12.2                         | ( $\bar{1}$ 0.748 0.496)        |
| AuCd     | 0.715   | 24.986                                  | 10.48                        | ( $\bar{1}$ 0.786 0.573)        |

**Table 4**

Energy-minimal lattice-parameters and lattice-offset triads determined from DFT to determine the equilibrium twin boundary structure on rational terraces.

| Material | Martensitic crystal structure (From DFT)                        | Cohesive energy, $E_{COH}$ (eV/atom) | Lattice-Motif atomic positions (from DFT)                              | Lattice-Offset triad ( $\bar{x}, \bar{y}, \bar{z}$ ) | TB Energy $E_{TB}$ ( $\frac{mJ}{m^2}$ ) |
|----------|---|--------------------------------------|--|--|---|
| TiPd     | $a = 4.899 \text{ Å}, b = 2.787 \text{ Å}, c = 4.576 \text{ Å}$ | -7.016                               | Ti (0, 0, 0), (0.403, 0, 0.5)<br>Pd (0.89, 0.5, 0.5), (0.513, 0.5, 0)  | (0.06, 0.450, 0.097)                                 | 189.8                                   |
| TiPt     | $a = 4.874 \text{ Å}, b = 2.764 \text{ Å}, c = 4.626 \text{ Å}$ | -7.837                               | Ti (0, 0, 0), (0.395, 0, 0.5)<br>Pt (0.885, 0.5, 0.5), (0.509, 0.5, 0) | (0.066, 0.446, 0.105)                                | 287.3                                   |
| AuCd     | $a = 5.009 \text{ Å}, b = 3.176 \text{ Å}, c = 4.899 \text{ Å}$ | -2.174                               | Cd (0, 0, 0), (0.409, 0, 0.5)<br>Au (0.504, 0.5, 0), (0.905, 0.5, 0.5) | (0.05, 0.454, 0.091)                                 | 211.4                                   |

2020; Pond and Hirth, 2018; Pond et al., 2019), found to be the smallest-norm difference-vector between two translational symmetry vectors in the twin and matrix variant. The translational symmetry vectors for the TBs considered are found to be  $\vec{t}_{tw} = [\bar{1}\bar{1}0]_{tw}$  and  $\vec{t}_M = [\bar{1}\bar{1}0]_M$ , thereby yielding the Burgers vector as:

$$\vec{b}_{tw} = [\bar{1}\bar{1}0]_{tw} - [\bar{1}\bar{1}0]_M \quad (11)$$

The translational symmetry vectors are indicated in a dichromatic pattern representing lattice vectors of both the matrix and the twin variant (with TiPd lattice as the exemplary case) in Appendix B. The Burgers vectors are all aligned with the direction of twinning shear  $\eta_1$  and their magnitudes are listed in Table 3. The step-height of the disconnection is given by:

$$h_D = |\vec{t}_M \cdot \hat{n}_T| = 2d_{(\bar{1}\bar{1}\bar{1})} \quad (12)$$

Thus, the step height of the disconnection spans two interplanar spacings between the  $K_T = (\bar{1}\bar{1}\bar{1})$  terrace-planes. The shear carried by the Burgers vector can be determined as  $|\vec{b}_{tw}|/h_D$ , found to be exactly equal to the terrace-shear  $s_T$ , i.e.

$$|\vec{b}_{tw}|/h_D = s_T \quad (13)$$

Thus, the Burgers vector of the twinning disconnection carries the terrace-shear  $s_T$ , defined in Section 2.3, and not the classical twinning shear  $s$ . The implications of this feature will be discussed in Section 3.

Finally, the irrationality of the Type II TBs are explained using the T-D model by deriving the spacing between the twinning disconnections and the Miller-index identity of the effective stepped topology. The twinning disconnections will be periodically spaced on the rational terrace such that their strain-field exactly cancels out the coherence-strains on the rational terrace. For the shear-mismatch strain on the rational terraces, an array of screw-dislocations with dislocation lines parallel to  $\eta_1$  will cancel out the coherence strain exactly. The spacing of these dislocations to nullify the strain is determined from the Frank-Bilby equation, given by:

$$\vec{B} = \vec{b}_{tw}/d = -\mathbf{E}_c \cdot \vec{v} = -(\mathbf{D}_{tw}^{-1} - \mathbf{D}_M^{-1}) \vec{v} \quad (14)$$

where  $\vec{v}$  is the vector perpendicular to the direction of the dislocation line, in this case perpendicular to  $\eta_1$  (refer Fig. 6). The tensor  $\mathbf{E}_c$  represents the three-dimensional coherence-strain-mismatch tensor between the matrix and the twin variant. The tensors  $\mathbf{D}_{tw,M}^{-1}$  represent the deformation gradients that map the coherently-strained state of the twin and matrix, respectively, to their unstrained states, given by the equations:

$$\mathbf{D}_{tw}^{-1} = \begin{pmatrix} 1 & -\gamma_T & 0 \\ 0 & 1 & 0 \\ 0 & 0 & 1 \end{pmatrix}; \mathbf{D}_M^{-1} = \begin{pmatrix} 1 & \gamma_T & 0 \\ 0 & 1 & 0 \\ 0 & 0 & 1 \end{pmatrix} \quad (15)$$

The disconnection spacing is consequently determined as:



$$d = \left| \vec{b}_{tw} \right| / 2\gamma_T \quad (16)$$

Consequently, the angle of inclination of the stepped topology is given by  $\theta = \tan^{-1} \frac{h_p}{d}$ . Both  $d$  and  $\theta$  are listed in Table 3 for all SMAs considered in this study. Note that the calculated angle of inclination  $\theta$  from the stepped topology is consistent with that of Eq. (3) in Section 2.1, employing the normal vectors of the rational terrace plane and irrational TB plane. The Miller-indices of the effective plane defined by the topology can be obtained from the reciprocal space lattice  $P_{LAT}^M$ , calculated from  $C_{LAT}^M$  through the Eq. (2). The indices are normalized such that one of the index is unity and listed in Table 4.

$$\begin{pmatrix} h \\ k \\ l \end{pmatrix} = (P_{LAT}^M)^{-1} \begin{pmatrix} 0 \\ -\sin\theta \\ \cos\theta \end{pmatrix} \quad (17)$$

Note that the effective Miller-indices of each T-D topology, given in column 5 of Table 3 closely reproduces the irrational identity of the Type-II TB in column 5 of Table 1.

## 2.5. Ab initio calculation of twin boundary energy

Finally, the energies of the Type II TBs are calculated. It has been shown recently that the atomistic potential energy on the rational terraces of the T-D topology strongly dominates the strain-energy of the array of disconnections and therefore decides the total TB energy (Mohammed and Sehitoglu, 2021). Therefore, in this section, a framework to establish the atomic-structure on the terrace is proposed and the energy is computed within a Density Functional Theory (DFT) framework using the Vienna Ab-initio Simulation Package (VASP) (Hafner, 2008). For the simulations, the pseudopotentials with Projector-Augmented-Wave (PAW) basis wave-functions and Perdew-Burke-Ernzerhof parametrization of Generalized-Gradient-Approximation (PBE-GGA) exchange-correlation functional were employed. First, the converged DFT parameters are determined, namely the plane-wave energy cut-off  $E_{CUT}$  and the number of  $k$ -points. Self-Consistent-Field (SCF) simulations are run on a B2 unit cell, with the lattice constant  $a_0$  chosen to be that measured by experiment (listed in Table 1). The energy tolerance for convergence of the SCF calculations was chosen to be 1 meV. The simulations are performed at increasing magnitudes of the energy cut-off  $E_{CUT}$  and the number of  $k$ -points until the total energy of the system converges within 5 meV/atom. The values of parameters at which this convergence is achieved are used for subsequent simulations of the TB atomic structure. The converged magnitudes of the plane-wave energy cut-off and the number of  $k$ -points are found to be  $E_{CUT} = 550$  eV and  $k_{CUT} = 12$  respectively (illustrated in Fig. 7). Note that, although results in Fig. 7 are illustrated from simulations on TiPd, individual simulations for each SMA system were performed and converged parameters were obtained. It was found that the set of values ( $E_{CUT} = 550$  eV,  $k_{CUT} = 12$ ) sufficed for all the systems considered in this study.

Next, the B19 orthorhombic lattice constants consistent with the chosen pseudopotentials must be determined. The procedure is described for TiPd in this section, and the same was applied for both TiPt and AuCd as well. First, the volume of the unit cell is determined by performing fixed-volume SCF calculations, results of which are given in Fig. 8(a). Then the individual ratios  $b/a$  and  $c/a$  are varied across a grid to determine the most energetically favorable pair, the results of which are illustrated in Fig. 8(b). With the energy-minimizing lattice constants,  $a, b, c$ , an ionic-relaxation is performed (with a force tolerance of 5 meV/Å) to determine the equilibrium atomic-positions within the B19 unit cell. Results of the DFT lattice constants and lattice-motif positions for the unit cell are listed in Table 4.

Having determined the lattice constants suitable for the simulations, the TB structure can now be determined. Note that both the atomic-structures of both the matrix and twin variants will be subject to the coherence-strains defined in Section 2.2 and defined by  $C_{LAT}^{M,C}$ ,  $C_{LAT}^{tw,C}$  respectively, defined by Eq. (6). First, a periodic simulation cell suitable for the TB structure must be defined. Since DFT calculations are expensive and scale quickly with the number of atoms, care must be taken to involve the least number of atoms in the structure. Owing to the non-cubic structure of the martensite, the simulation cell is found to be triclinic, illustrated in figure 9(a). The bounding box vectors  $\vec{L}_1 - \vec{L}_2 - \vec{L}_3$  are defined with reference to the same orthonormal coordinate system  $\hat{e}_1 - \hat{e}_2 - \hat{e}_3$  (defined in Fig. 3 in Section 2.2). The vector components for these vectors are obtained through the matrix  $C_{LAT}^{M,C}$  defined in Eq. (6). For instance, the

vector  $\vec{L}_2 = [110]_M$  has the components  $C_{LAT}^{M,C} \begin{pmatrix} 1 \\ 1 \\ 0 \end{pmatrix}$ , and the other vectors  $\vec{L}_1 = [121]$ ,  $\vec{L}_3 = 4[\bar{1}\bar{1}\bar{1}]_M$  are determined similarly. There

is no subscript on  $[121]$  as it is identical in both the matrix and the twin variants. The vector  $\vec{L}_2$  is aligned with  $[011]_{tw}$  in the coherently-strained twin crystal structure. A total of  $12 K_T = (\bar{1}\bar{1}\bar{1})$  planes are simulated with  $N = 6$  planes corresponding to the twin variant, remaining 6 to the matrix variant, and with each plane containing 4 atoms (shown in Fig. 9(b)). To incorporate  $N$  twin planes, the vector  $\vec{L}_3$  must be incremented by  $Ns_T d_{(\bar{1}\bar{1}\bar{1})}$ , where  $d_{(\bar{1}\bar{1}\bar{1})}$  is the interplanar spacing, accounting for the presence of the terrace-shear in the system (figure 9(b)). This is necessary as without this shear, the periodicity across the top and bottom boundaries of the simulation cell would be broken precluding an accurate simulation of the twinned structure.

Having defined the simulation cell, the TB structure can now be determined. The crystallography of the  $K_T$  terrace is not atomically flat as noted previously in Fig. 5. Furthermore, the atomic-positions in the matrix and twin are not commensurate with each other precluding the construction of the TB as a common plane between the variants (refer figure 9(c)). The atomic-structure must be unambiguously defined by determining the relative position of the twin variant with respect to the matrix. This relative position is



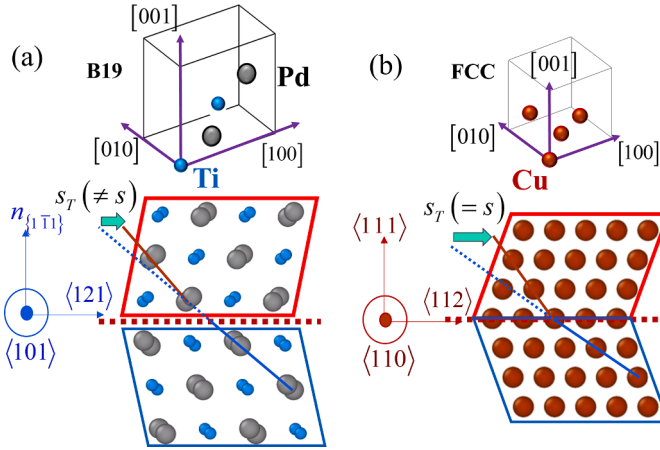


**Fig. 5.** Physical significance of the distinction between twinning-shear  $s$  and terrace-shear  $s_T$ : (a) the terrace-shear  $s_T$  describes the shear on the coherently-strained rational-terrace of the Type II twin in B19 orthorhombic TiPd, and this shear is distinct from the classical twinning shear  $s$ . (b) Such a distinction is absent and thus cannot be inferred from twinning behavior of highly-symmetric crystal structures such as  $\{111\}$  twinning in Face-Centered Cubic (FCC) materials e.g. Cu, as shown.

otherwise termed as the “lattice-offset”, defined and determined for the TBs considered as follows. Two reference origin points  $O_{tw}$  and  $O_M$  are chosen on the lattice-sites of two crystallographic planes  $P_{tw}$  and  $P_M$ , shown in figure 10(a). Recall that the lattice and motif sites were defined in Section 1. The plane  $P_{tw}$  lies on the twin variant and  $P_M$  is a virtual crystallographic plane that were to exist if the matrix variant was presumed to extend by one more plane into the twin. The triad vector  $(x, y, z)$  describing the relative position of  $O_T$  with respect to  $O_M$  defines the lattice-offset vector that needs to be determined. Given the periodicity of the lattice, the vector can be defined in a normalized form given by:

$$\bar{x} = \frac{x}{|[121]|}; \bar{y} = \frac{y}{|[10\bar{1}]|}; \bar{z} = \frac{z}{d_{(\bar{1}\bar{1}\bar{1})}} \quad (18)$$

where  $d_{(\bar{1}\bar{1}\bar{1})}$  is the interplanar spacing of the  $(\bar{1}\bar{1}\bar{1})$  planes. The components  $(\bar{y}, \bar{z})$  can be determined based on two considerations:

- The volume must be conserved during twinning, therefore requiring the interplanar spacing to be preserved as one moves from the matrix to the twin. This determines  $\bar{z}$ .
- The crystal structure of the matrix and the twin would look identical when seen along the direction of twinning  $\eta_1 = [121]$ . This determines  $\bar{y}$ .

The magnitude of  $\bar{x}$  however requires atomistic simulation and is not known apriori. At incremental magnitudes of  $\bar{x}$  between 0 and 1, an SCF simulation is performed to determine the potential energy of the atomic-structure at that offset. The magnitude of  $\bar{x}$  that yields the lowest energy is determined. The results are plotted in figure 10(c). The relative changes in the TB potential energy are plotted with respect to the energy at zero-offset i.e. at  $\bar{x} = 0$ . Non-trivial lattice-offsets were found and are reported in Table 4, determined to within  $\pm 0.01$ . These findings of non-trivial lattice-offsets are consistent with prior results in NiTi as reported in ref. (Mohammed and Sehitoglu, 2020b). Thus without the simulation of the energetics, there is no basis on which a reliable choice for  $\bar{x}$  can be made apriori. Determination of the lattice-offset unambiguously defines the relative position of the twin variant with respect to the matrix and completes definition of the TB structure on the rational terrace. The resulting TB structure is equilibrated following the conjugate-gradient scheme, specifying the force-tolerance for convergence as 5 meV/Å. The energy of the relaxed atomic-structure is used to obtain the planar TB energy  $E_{TB}$ , and the results are reported in Table 4.

### 3. Discussions

The purpose of this study is to explain the irrationality of Type II TBs in three SMAs through the Terrace-Disconnection (T-D) structure and to calculate their energies from ab initio calculations. And by doing so, it is expected that further generalized characteristics of this TB could be deciphered. In the well-studied NiTi system, research on the Type II TB has greatly benefited from the availability of extensive experimental results, postulates regarding the possible rational terrace, and the availability of interatomic potentials for atomistic simulations (Knowles, 1982; Knowles and Smith, 1981; Ko et al., 2015; Liu and Xie, 2003, 2006; Nishida et al., 2008a, 1995a, 1995b; Ren and Sehitoglu, 2016; Xie and Liu, 2004; Zhong et al., 2011). In moving beyond this system and examining other Type II TBs, the conspicuous absence of similar groundwork posed multiple challenges associated with definition of the rational terrace plane, the physical origins of the coherence strains, and choice of a suitable atomistic framework to determine the TB energy. This study proposes to resolve these challenges and gleans certain generalized characteristics of Type II TBs that would be of both

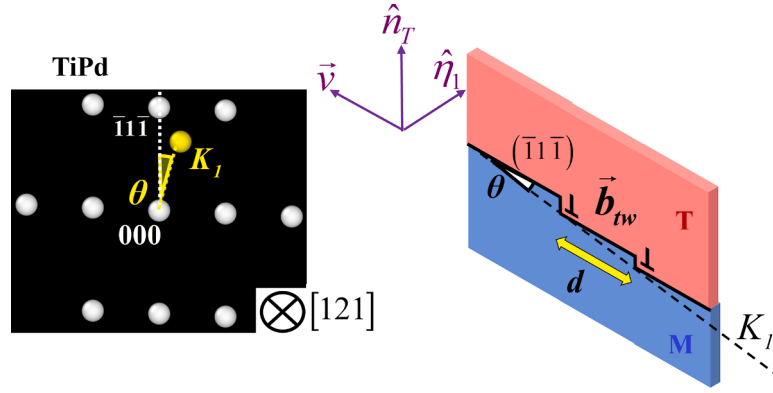


**Fig. 6.** Terrace-Disconnection topology of Type II Twin Boundary, with periodic array of twinning disconnections  $\vec{b}_{tw}$  with spacing  $d$ ; the angle of deviation  $\theta$  between the irrational plane and the rational-terrace initially seen in the reciprocal lattice is reproduced in the T-D topology.

scientific relevance in the field of twinning and of technological relevance in SMA materials.

The first challenge in studying the Type II TBs is the definition of the rational terrace. On first look, it is not trivial to determine the rational terrace for all the irrational TBs listed in Table 2. For instance, in TiPd, the rational terrace for irrational plane  $(\bar{1} \ 0.6780 \ 356)$  could be postulated as either  $K_T = (\bar{1}1\bar{1})$  or  $K_T = (\bar{1}10)$ . An objective approach was proposed in Section 2.1 where the rational-terrace could be determined by visualizing the discrete reciprocal space lattice, and proposing the terrace to be the nearest rational-plane to the irrational  $K_1$  TB, immediately noting the preference of  $(\bar{1}1\bar{1})$  over  $(\bar{1}10)$ . Note that this approach, in effect, only finds the rational-terrace with a normal closest to the irrational plane. Although simple, there is an important challenge that this approach overcomes. When it comes to the choice of rational terraces, one could always choose a better rational-approximation, say  $K_T = (53\bar{1})$  or  $K_T = (753)$ . The normals to these terraces would indeed be closer to the normal to  $K_1$ . However, their high Miller-indices imply the atomic-densities on these planes would be low and a low planar density would lead to higher atomistic potential energy of the TB. In fact, this was recently illustrated explicitly in NiTi (Mohammed and Sehitoglu, 2021), where the potential energy of a low-index rational plane was shown to have much lower potential energy than a higher-index rational plane, using Molecular Statics simulations. Therefore, it is energetically preferable for the rational terrace to have the *least possible* Miller indices. By visualizing the reciprocal space lattice points, the least-index planes closest to  $K_1$  can be unambiguously determined by focusing only on the lattice-points closest to the central 000 zone (refer Fig. 2(a)).

Once the rational terrace is determined, the required coherence-strains on the terrace can be determined by examining the crystallography as illustrated in Section 2.2. The necessity of atomic-registry on the terrace dictates the alignment of crystallographic vectors  $\vec{v}_M = [10\bar{1}]_M$  and  $\vec{v}_{tw} = [\bar{1}01]_{tw}$ , revealing the requirement of coherence-strain  $\gamma_T$ . Though from a continuum mechanics standpoint, it is a necessary question to ask where this strain originates from. For the first time, a partitioning between the terrace coherence-strain and terrace-shear is shown in Section 2.3, resulting from a simple rotational transformation of the twinning deformation gradient. This partitioning is necessary to understand since, on the terrace, the shear that transforms the matrix to the twin is indeed the terrace-shear and not the twinning-shear (illustrated in Fig. 5). This effect is also illustrated in the calculated Burgers vector of the twinning disconnection in Section 2.4. The Burgers vector was determined from a difference of lattice-symmetry vectors, and the calculated magnitude turns out to be a multiple of  $s_T$  and not  $s$ . Therefore, as the Burgers vector sweeps through the terrace, it carries the shear of  $b_{tw}/h_D = s_T$  i.e. the terrace-shear and not the twinning shear. Such an understanding could not have been achieved from more common Compound twins in FCC materials or even rational Type I twins in SMAs, where neither coherence strains nor a distinct terrace-shear is required. It was the challenge of irrationality of the Type II TBs and consequent necessity of the T-D topology that has led to this understanding.

Furthermore, in the absence of a reliable interatomic potential, a formal procedure to determine the atomic-structure on the rational terraces of Type II TBs is offered within a DFT framework, in Section 2.5. The lattice-offsets are critical to establish the correct TB structure and consequently the TB energy. For non-single-lattice structures, as considered in this study and as prevalent in multiple other martensitic phases of SMAs, these offsets overcome the ambiguity in determining the TB given the incommensurate and non-flat atomic-structures of the twinning planes (for instance on the  $(\bar{1}1\bar{1})$  terrace-planes in this case). These offsets, particularly  $\bar{x}$ , cannot be determined without a simulation of the energetics of the TB. The importance of such offsets has been noted in crystal structures beyond SMAs as well, such as in Hexagonal Close-Packed (HCP) materials (Gengor et al., 2021). Note that the calculated TB energies in Table 4 are generally higher than that of conventional FCC twins such as for  $\{111\}$  twins in FCC Copper, where  $\gamma_{TB} \sim 24 \text{ mJ/m}^2$  (Mishin et al., 2001). This can be expected for the complex martensitic structure of the binary alloys considered, as also seen previously in the well-studied NiTi system with relatively high TB energy (Ezaz and Sehitoglu, 2011; Ezaz et al., 2011), and detwinning stress (Nishida et al., 1998; Sittner et al., 2020). There may also be contributions from the individual atomic species involved, for instance, similar magnitudes of TB energies were predicted in HCP Ti (Gengor et al., 2021, 2023) with relatively high twinning stress calibrated from experiments (Ma et al., 2019). Additionally, calculated TB energies and twinning stress in FCC Pd, Pt, are also higher than in Cu (Kibey et al., 2007). A complete assessment of the driving factors dictating the magnitude of TB energies, although out of scope for the present

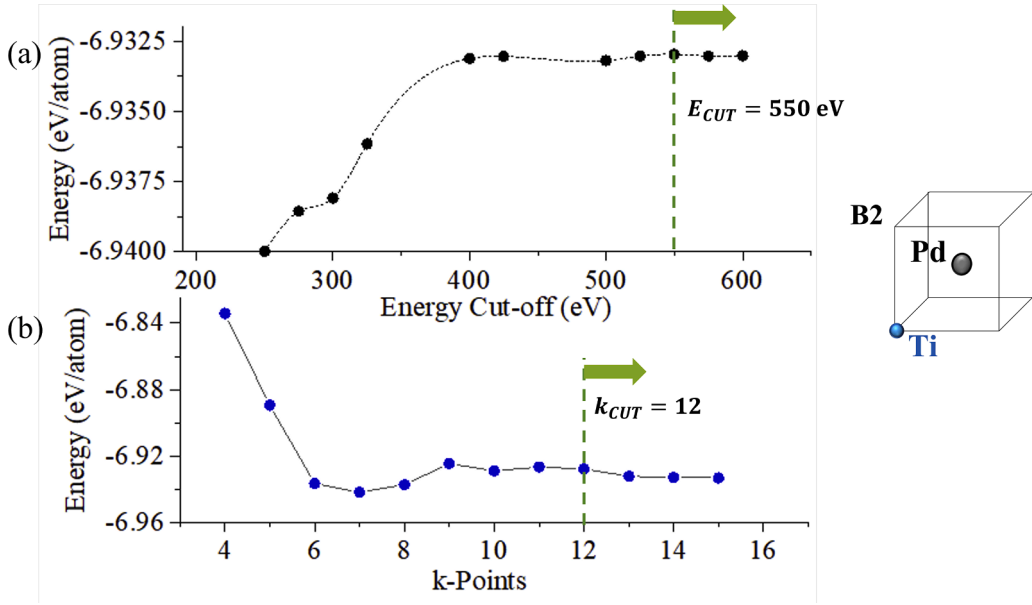


**Fig. 7.** DFT parameters for simulations of lattice-offset and twin boundary energy: (a) Energy cut-off  $E_{CUT}$  and (b) number of k-points; the B2 simulation cell used for the simulations is illustrated, with the example of TiPd.

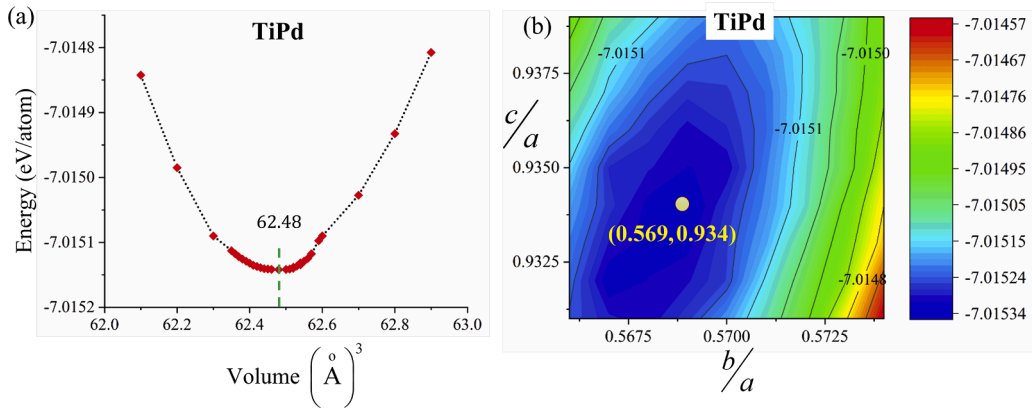


**Fig. 8.** Determination of (a) B19 unit-cell volume and (b) B19 lattice-parameter ratios of orthorhombic cell of TiPd.

study, would be a worthwhile topic for further research, evaluating factors such as the specific atomic species involved, the planar ionic density on the rational terrace plane, and distribution of the electron-density.

Section 2.4 establishes how the T-D topology sufficiently explains the irrationality of all Type II TBs considered in this study. Thus, the T-D structural model proposed in this study is defined by the topology derived in Section 2.4 (refer Fig. 6) and the terrace atomic-structure constructed through DFT in Section 2.5 (refer Fig. 10). The twinning-disconnections are spaced such that they nullify the coherence-strain at the terrace,  $\gamma_T$ , in the far-field away from the TB. Recall from previous discussion that the twinning-disconnections only carry the terrace-shear  $s_T$ . Both these points reveal an elegance behind the adoption of the T-D topology by the TB. This is illustrated in Fig. 11 below. In Fig. 11(a), the classical notion is illustrated. By this notion, for minimum strain-energy from a continuum-mechanics standpoint, the twin plane must inhabit an invariant plane shared between the twin and matrix so that there are no strain-energies in the system and both the crystal-structures are in their un-strained native configurations. This requirement leads to determination of the invariant plane  $K_1$  as having an irrational Miller-index identity, and the twinning shear  $s$  necessary to transform the matrix to the twin. However, here lies the catch. The irrational plane, while a perfectly plausible continuum entity, is not an energetically favorable atomic-plane for the TB. If the TB were to reside on such a plane it would have to pay the cost of a high atomistic potential energy. This is not preferred by the material and instead an alternative route is taken. The interface adopts a T-D topology where there are rational terraces that are strained into coherence, with coherence-strains  $\gamma_T$ . By inhabiting a low-index rational terrace, the atomistic potential energy is minimized, at the cost of the continuum strain-energy of having coherence-strains. However, these strains-are relieved by a periodic arrangement of twinning-disconnections on the rational-terrace. Note that when the twin-migrates,

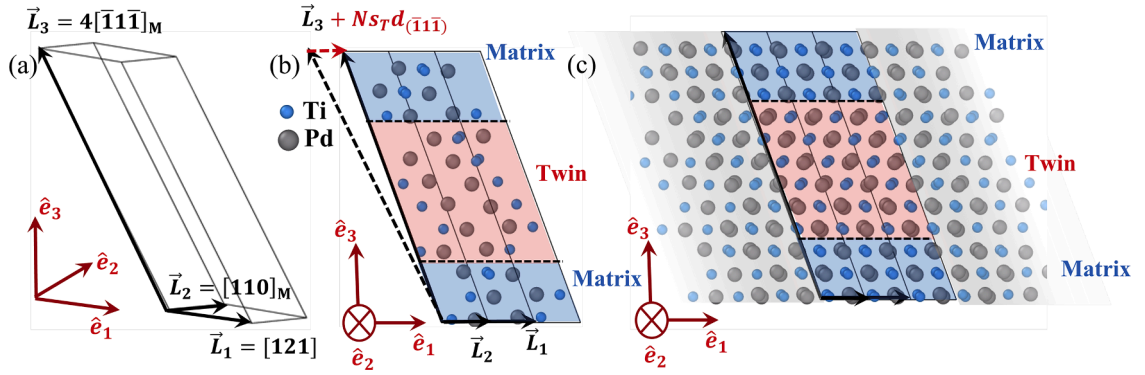


**Fig. 9.** Construction of simulation cell in DFT for analysis of twinned structure: (a) Triclinic simulation cell with lattice vectors  $\vec{L}_1 - \vec{L}_2 - \vec{L}_3$  defined in an orthonormal basis  $\hat{e}_1 - \hat{e}_2 - \hat{e}_3$ ; this cell is suitable to construct a single pure variant of the matrix crystal structure (b) Twinned structure constructed within simulation cell, where the vector  $\vec{L}_3$  is corrected with the applied terrace-shear,  $s_T$  based on the number of twin-planes (with interplanar spacing  $d_{\{111\}}$ ) included in the simulation cell,  $N$ ; there are 4 atoms per  $\{111\}$  plane within this cell (c) Twinned structure illustrated with multiple periodic images across the periodic boundaries, illustrated only for visualization (the actual simulation cell employed has 4 atoms per plane).

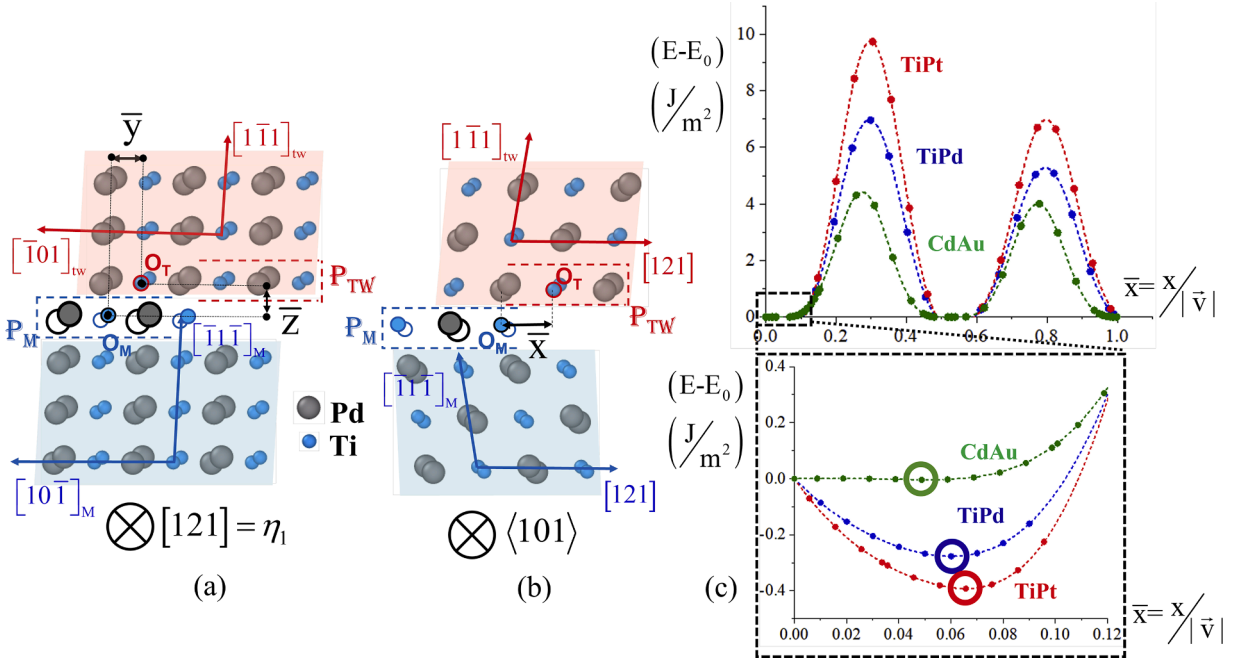


**Fig. 10.** Determination of lattice-offset for construction of twin boundary structure: Defining the normalized lattice-offsets (a)  $(\bar{y}, \bar{z})$  and (b)  $\bar{x}$ ; the energy-minimizing offset is determined from DFT simulations, results of which are shown in (c) ( $E$  is the potential energy at a general offset  $\bar{x}$  and  $E_0$  is the energy at offset  $\bar{x} = 0$ ).

the twinning disconnections only carry a part of the classical twinning shear  $s$ , and it is only the terrace-shear  $s_T$ . By relieving the strain-energy in the bulk, the additional cost of continuum strain-energy is minimized to a magnitude near insignificant compared to the gained reduction of atomistic potential energy in preferring a rational terrace. Thus, the picture of twinning changes from a continuum-compatible  $(K_1, s)$  description to a continuum- and atomistic-compatible  $(K_T, s_T, \gamma_T)$  picture as shown in Fig. 11(b). In summary, the T-D topology is, in a manner of speaking, the material's solution to exhibiting an effective irrational plane by involving atomistically-favorable rational terraces and continuum-favorable periodic disconnections relieving far-field strains.

The proposed topological characteristics of Type II TBs serve to clarify the internal twin interface structure in the martensite phase of SMAs where Type II twins are prevalent as a LID mode. Such an understanding serves as a pre-requisite to subsequently examine the irrational nature of the austenite-martensite phase-transformation front, where the internal martensitic twin interfaces meet the parent austenite phase. In addition, the importance of these internal TBs in causing transformation-induced slip on austenitic slip-planes

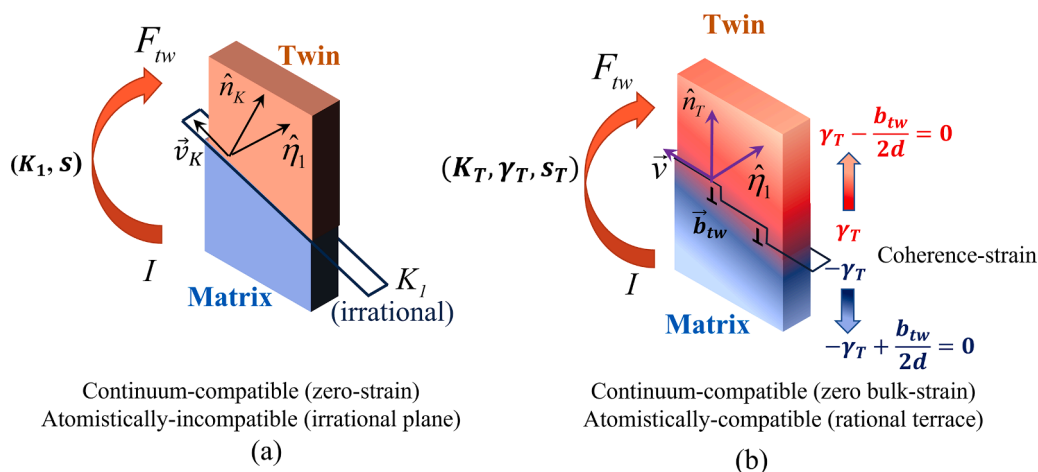


**Fig. 11.** Physical significance of the Terrace-Disconnection (T-D) topology for Type II TB: (a) In the classical twinning description, the twinning shear  $s$  is applied on the irrational twinning plane  $K_1$ ; this structure would yield zero continuum strain-energy but implies a higher atomistic potential energy on the irrational plane. (b) The T-D topology achieves an effective compromise where there are coherence-strains  $\gamma_T$  sustained on a rational terrace  $K_T$ , subsequently nullified by a periodic arrangement of twinning disconnections  $\vec{b}_{tw}$ , ultimately attributing a stepped nature that explains the irrational indices.

aligned with the TB plane has long been known (Kajiwara and Kikuchi, 1982; Kajiwara and Owen, 1973; Mohammed and Sehitoglu, 2020a; Norfleet et al., 2009; Simon et al., 2010; Zhang et al., 2012). A clear understanding of the irrational TB identity of Type II twins would now help to unambiguously identify the rational terraces and corresponding twinning disconnections mechanistically relevant for slip-emission. The validity of the proposed T-D topology can be verified for the considered SMAs and twin systems much in the same way as it was done for NiTi in the past (Hirth and Wang, 2021; Hirth et al., 2023; Knowles, 1982; Liu and Xie, 2003; Mohammed and Sehitoglu, 2020b, 2021; Shilo et al., 2021; Xie and Liu, 2004). In NiTi, the T-D topology for the Type-II twin interface  $K_1 = \{0.7205 \ 1 \ \bar{1}\}$  was proposed from High-Resolution Transmission Electron Microscopy (HRTEM) observations of the interface, identifying the  $K_T = \{11\bar{1}\}$  rational terrace plane and periodic disconnections (Knowles, 1982; Liu and Xie, 2003; Xie and Liu, 2004). Similar experimental studies focused on the Type II systems considered in this study would be promising directions of future research. From a modeling standpoint, another promising direction for future research would be to simulate the complete atomic-structure of the irrational interface by assembling multiple terrace-structures spaced by disconnections following the T-D topology. Such a study would however require a large number of atoms making it computationally infeasible for the current DFT-based approach and necessitating the use of Molecular Statics/Dynamics (MS/MD) frameworks relying on empirical interatomic potentials.

## 4. Conclusions

This study focuses on Type II twins in 3 SMA systems – TiPd, TiPt and AuCd - exhibiting B19 orthorhombic martensitic crystal structures. The Type II twin interfaces exhibit irrational identities and are conjugate to the rational  $\{111\}$  Type I twin mode in these systems. The irrational identities of all TBs are explained using the T-D topology revealing novel general characteristics exhibited by this type of TB. It is shown that the choice of rational terrace comes from the reciprocal space of the crystal lattice and that the terrace should be a low-index plane to have the highest planar atomic-density. The origin of the coherence strain on the terrace is shown from both a crystallographic standpoint and from a continuum kinematics standpoint. The continuum perspective reveals the partitioning of the classical twinning shear  $s$  on the irrational plane  $K_1$  to coherence-strain and terrace-shear ( $\gamma_T, s_T$ ) components on the T-D topology. The Burgers vector of the twinning disconnection was determined from a crystallographic approach involving translational symmetry vectors, and it is shown for the first time that the Burgers vector carries the terrace-shear  $s_T$  and not the twinning shear  $s$ , on the rational terrace  $K_T$ . The spacing of the twinning disconnections on the terrace is calculated from the Frank-Bilby equation, closely reproducing the irrational Miller-index identity of the Type II TB. The atomic-structure on the rational-terraces are determined from DFT calculations establishing formal procedures to construct TB structures within the simulation framework. The energy-minimizing lattice-offsets are determined to construct the TB structure on the terrace, ultimately leading to determination of the total TB energy. A novel perspective on the energetic preference of the T-D topology by the Type II TB is forwarded, discussing how the topology balances both the continuum-energy and atomistic-energy considerations. Such an understanding could not have been achieved from rational TBs such as Compound twins in FCC materials or Type I twins in SMAs and is a necessary advancement in understanding the energetics of twin interfaces.

## CRedit authorship contribution statement

**Ahmed Sameer Khan Mohammed:** Writing – original draft, Methodology, Investigation, Conceptualization. **Huseyin Sehitoglu:**

Writing – review & editing, Supervision, Funding acquisition, Conceptualization.

### Declaration of competing interest

The authors declare that they have no known competing financial interests or personal relationships that could have appeared to influence the work reported in this paper.

### Data availability

Data will be made available on request.

### Acknowledgments

The work is supported by the Air Force Office of Scientific Research (AFOSR) under award number FA9550-18-1-0198 and partly by the National Science Foundation (NSF) under award numbers 2125821 and 2104971, which are gratefully acknowledged. The use of the Illinois Campus Cluster, a computing resource that is operated by the Illinois Campus Cluster Program (ICCP) in conjunction with the National Center for Supercomputing Applications (NCSA) and which is supported by funds from the University of Illinois at Urbana-Champaign, is also gratefully acknowledged.

### Appendix A. Crystallographic calculation of irrational indices of Type II TBs

The formulae for calculation of the irrational indices of  $K_1$  twin-plane (refer Table 1) are presented in this appendix. The reader is directed to the classical work of ref. (Jaswon and Dove, 1960) for a detailed exposition of the theory. The irrational indices can be calculated from the lattice-parameters ( $a, b, c$  in Table 1), the indices of the direction of twinning  $\eta_1 = [pqr]$ , and the rational indices of the conjugate Type I twinning mode  $K_2 = (hkl)$ . In this study,  $p = 1, q = 2, r = 1, h = 1, k = 1, l = 1$ . The irrational indices for  $K_1 = (h'k'l')$  can be computed from the formulae below and normalized:

$$\begin{aligned} h' &= h - (ph + qk + lr)(a^2p) / (a^2p^2 + b^2q^2 + c^2r^2) \\ k' &= k - (ph + qk + lr)(b^2q) / (a^2p^2 + b^2q^2 + c^2r^2) \\ l' &= l - (ph + qk + lr)(l^2r) / (a^2p^2 + b^2q^2 + c^2r^2) \end{aligned} \quad (19)$$

### Appendix B. Illustration of translational symmetry vectors and Burgers vector

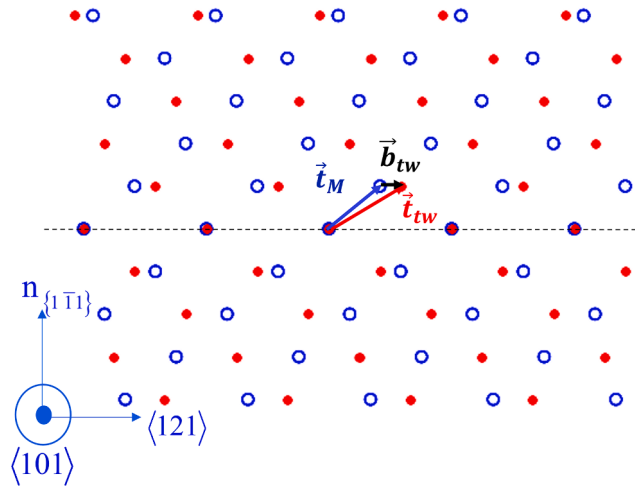


**Fig. B1.** Illustration of translational symmetry vectors  $\vec{t}_{tw}$ ,  $\vec{t}_M$ , and Burgers vector  $\vec{b}_{tw}$ , in a dichromatic pattern representing lattice vectors of the coherently strained matrix and twin variants; the open blue circles correspond to the lattice points of the matrix variant whereas the filled red circles represent that of the twin variant.



## References

- Adachi, K., Perkins, J., Wayman, C.M., 1986. Type II twins in self-accommodating martensite plate variants in a Cu-Zn-Al shape memory alloy. *Acta Metallurgica* 34, 2471–2485.
- Alkan, S., Chowdhury, P., Sehitoglu, H., Rateick, R.G., Maier, H.J., 2016. Role of nanotwins on fatigue crack growth resistance – experiments and theory. *Int. J. Fatigue* 84, 28–39.
- Beyerlein, I.J., Zhang, X., Misra, A., 2014. Growth twins and deformation twins in metals. *Annu. Rev. Mater. Res.* 44, 329–363.
- Bilby, B.A., Crocker, A.G., 1965. The theory of the crystallography of deformation twinning. *Proc. R. Soc. Lond. Ser. A. Math. Phys. Sci.* 288, 240–255.
- Blömers, C., Lepsa, M.I., Luysberg, M., Grützmacher, D., Lüth, H., Schäpers, T., 2011. Electronic Phase Coherence in InAs Nanowires. *Nano Lett.* 11, 3550–3556.
- Bönisch, M., Wu, Y., Sehitoglu, H., 2018a. Hardening by slip-twin and twin-twin interactions in FeMnNiCoCr. *Acta Mater.* 153, 391–403.
- Bönisch, M., Wu, Y., Sehitoglu, H., 2018b. Twinning-induced strain hardening in dual-phase FeCoCrNiAl<sub>0.5</sub> at room and cryogenic temperature. *Sci. Rep.* 8, 10663.
- Bucsek, A.N., Pagan, D.C., Casalena, L., Chumlyakov, Y., Mills, M.J., Stebner, A.P., 2019. Ferroelastic twin reorientation mechanisms in shape memory alloys elucidated with 3D X-ray microscopy. *J. Mech. Phys. Solids* 124, 897–928.
- Celebi, O.K., Mohammed, A.S.K., Krogstad, J.A., Sehitoglu, H., 2022. Evolving dislocation cores at Twin Boundaries: theory of CRSS Elevation. *Int. J. Plastic.* 148, 103141.
- Chowdhury, P., Sehitoglu, H., Maier, H.J., Rateick, R., 2016a. Strength prediction in NiCo alloys – the role of composition and nanotwins. *Int. J. Plastic.* 79, 237–258.
- Chowdhury, P., Sehitoglu, H., Rateick, R., 2016b. Recent advances in modeling fatigue cracks at microscale in the presence of high density coherent twin interfaces. *Curr. Opin. Solid State Mater. Sci.* 20, 140–150.
- Christian, J.W., Mahajan, S., 1995. Deformation twinning. *Prog. Mater. Sci.* 39, 1–157.
- Donkersloot, H.C., Van Vucht, J.H.N., 1970. Martensitic transformations in gold-titanium, palladium-titanium and platinum-titanium alloys near the equiatomic composition. *J. Less Common Metals* 20, 83–91.
- Dwight, A.E., Conner Jnr, R.A., Downey, J.W., 1965. Equiatomic compounds of the transition and lanthanide elements with Rh, Ir, Ni and Pt. *Acta Crystallogr.* 18, 835–839.
- Ezaz, T., Sehitoglu, H., 2011. Type II detwinning in NiTi. *Appl. Phys. Lett.* 98, 141906.
- Ezaz, T., Sehitoglu, H., Maier, H.J., 2011. Energetics of twinning in martensitic NiTi. *Acta Mater.* 59, 5893–5904.
- Gengor, G., Mohammed, A.S.K., Sehitoglu, H., 2021. {101<sup>-</sup>2} Twin interface structure and energetics in HCP materials. *Acta Mater.* 219, 117256.
- Gengor, G., Mohammed, A.S.K., Sehitoglu, H., 2023. The complexity of {112<sup>-</sup>1} twin interface structure and energetics in HCP materials. *Acta Mater.* 255, 119040.
- Gong, M., Graham, J., Taupin, V., Capolungo, L., 2021. The effects of stress, temperature and facet structure on growth of {101<sup>-</sup>2} twins in Mg: a molecular dynamics and phase field study. *Acta Mater.* 208, 116603.
- Gong, M., Ma, H., Yang, K., Liu, Y., Nie, J.-F., Wang, J., 2022. Symmetric or asymmetric glide resistance to twinning disconnection? *npj Comput. Mater.* 8, 168.
- Hafner, J., 2008. Ab-initio simulations of materials using VASP: density-functional theory and beyond. *J. Comput. Chem.* 29, 2044–2078.
- Hara, T., Ohba, T., Miyazaki, S., Otsuka, K., 1992. Electron Microscopy Study of Type II Twins in  $\gamma$ -Cu-Al-Ni Martensite. *Mater. Trans.* 33, 1105–1113. JIM.
- Heczko, O., 2014. Understanding motion of twin boundary—a key to magnetic shape memory effect. *IEEE Trans. Magn.* 50, 1–7.
- Hirth, J.P., Hirth, G., Wang, J., 2020. Disclinations and disconnections in minerals and metals. *Proc. Natl. Acad. Sci.* 117, 196–204.
- Hirth, J.P., Pond, R.C., 1996. Steps, dislocations and disconnections as interface defects relating to structure and phase transformations. *Acta Mater.* 44, 4749–4763.
- Hirth, J.P., Wang, J., 2021. Extension of the classical theory for types I and II twinning. *J. Mater. Res.* 36, 2615–2622.
- Hirth, J.P., Xie, D., Hirth, G., Wang, J., 2023. Recovery and facets for deformation twins in minerals and metals. *Proc. Natl. Acad. Sci.* 120, e2215085120.
- Huang, X., Rabe, K.M., Ackland, G.J., 2003. First-principles study of the structural energetics of PdTi and PtTi. *Phys. Rev. B* 67, 024101.
- Jaswon, M.A., Dove, D.B., 1960. The crystallography of deformation twinning. *Acta Crystallogr.* 13, 232–240.
- Jozaghi, T., Samimi, P., Chumlyakov, Y., Karaman, I., 2022. Role of thermally-stable deformation twins on the high-temperature mechanical response of an austenitic stainless steel. *Mater. Sci. Eng.: A* 845, 143199.
- Kajiwara, S., Kikuchi, T., 1982. Dislocation structures produced by reverse martensitic transformation in a Cu-Zn alloy. *Acta Metallurg.* 30, 589–598.
- Kajiwara, S., Owen, W.S., 1973. Substructure of austenite formed by a partial reverse martensitic transformation in an Fe-Pt alloy. *Metallurg. Trans.* 4, 1988–1990.
- Karki, B., Müllner, P., Pond, R., 2020. Topological model of type II deformation twinning in 10M Ni-Mn-Ga. *Acta Mater.*
- Kibey, S., Liu, J.B., Johnson, D.D., Sehitoglu, H., 2007. Predicting twinning stress in fcc metals: linking twin-energy pathways to twin nucleation. *Acta Mater.* 55, 6843–6851.
- Kim, Y.-K., Kim, H.-K., Jung, W.-S., Lee, B.-J., 2017. Development and application of Ni-Ti and Ni-Al-Ti 2NN-MEAM interatomic potentials for Ni-base superalloys. *Comput. Mater. Sci.* 139, 225–233.
- Knowles, K.M., 1982. A high-resolution electron microscope study of nickel-titanium martensite. *Philos. Mag. A* 45, 357–370.
- Knowles, K.M., Smith, D.A., 1981. The crystallography of the martensitic transformation in equiatomic nickel-titanium. *Acta Metallurgica* 29, 101–110.
- Ko, W.-S., Grabowski, B., Neugebauer, J., 2015. Development and application of a Ni-Ti interatomic potential with high predictive accuracy of the martensitic phase transition. *Phys. Rev. B* 92, 134107.
- Li, Q., Gong, M., Jiang, J., Chen, Y., Ma, H., Wu, Y., Hu, Y., Liu, Y., Liu, G., Wang, J., Zeng, X., 2023. Atomic-level quantification of twinning shears in magnesium alloy. *Acta Mater.* 246, 118665.
- Lieberman, D.S., Wechsler, M.S., Read, T.A., 1955. Cubic to orthorhombic diffusionless phase change— experimental and theoretical studies of AuCd. *J. Appl. Phys.* 26, 473–484.
- Liu, D.Z., Dunne, D., 2003. Atomic force microscope study of the interface of twinned martensite in copper–aluminium–nickel. *Scr. Mater.* 48, 1611–1616.
- Liu, Y., Xie, Z.L., 2003. Twinning and detwinning of {011} type II twin in shape memory alloy. *Acta Mater.* 51, 5529–5543.
- Liu, Y., Xie, Z.L., 2006. The rational nature of Type II twin in NiTi shape memory alloy. *J. Intell. Mater. Syst. Struct.* 17, 1083–1090.
- Lu, K., 2016. Stabilizing nanostructures in metals using grain and twin boundary architectures. *Nature Rev. Mater.* 1, 16019.
- Ma, C., Wang, H., Hama, T., Guo, X., Mao, X., Wang, J., Wu, P., 2019. Twinning and detwinning behaviors of commercially pure titanium sheets. *Int. J. Plastic.* 121, 261–279.
- Mishin, Y., Mehl, M.J., Papaconstantopoulos, D.A., Voter, A.F., Kress, J.D., 2001. Structural stability and lattice defects in copper: ab initio, tight-binding, and embedded-atom calculations. *Phys. Rev. B* 63, 224106.
- Mohammed, A.S.K., Sehitoglu, H., 2020a. Martensitic twin boundary migration as a source of irreversible slip in shape memory alloys. *Acta Mater.* 186, 50–67.
- Mohammed, A.S.K., Sehitoglu, H., 2020b. Modeling the interface structure of type II twin boundary in B19' NiTi from an atomistic and topological standpoint. *Acta Mater.* 183, 93–109.
- Mohammed, A.S.K., Sehitoglu, H., 2021. Strain-sensitive topological evolution of twin interfaces. *Acta Mater.* 208, 116716.
- Morii, K., Ohba, T., Otsuka, K., Sakamoto, H., Shimizu, K., 1991. Crystallography of  $\beta 2 \rightarrow \gamma 2'$  martensitic transformation in Au-47.5 at.% Cd and Au-47.5 at.% Cd-Cu alloys. *Acta Metallurgica et Materialia* 39, 2719–2725.
- Müllner, P., 2019. Twinning stress of type I and type II deformation twins. *Acta Mater.* 176, 211–219.
- Müllner, P., Chernenko, V.A., Kosterz, G., 2003. Stress-induced twin rearrangement resulting in change of magnetization in a Ni–Mn–Ga ferromagnetic martensite. *Scr. Mater.* 49, 129–133.
- Murallas, M., Park, S.-D., Kim, S.Y., Lee, B., 2017. Phase transformations, detwinning and superelasticity of shape-memory NiTi from MEAM with practical capability. *Comput. Mater. Sci.* 130, 138–143.
- Nishida, M., Hara, T., Matsuda, M., Li, S., 2008a. Crystallography and morphology of various interfaces in Ti–Ni, Ti–Pd and Ni–Mn–Ga shape memory alloys. *Mater. Sci. Eng.* 18–27. A 481–482.

- Nishida, M., Hara, T., Morizono, Y., Ikeya, A., Kijima, H., Chiba, A., 1997. Transmission electron microscopy of twins in martensite in TiPd shape memory alloy. *Acta Mater.* 45, 4847–4853.
- Nishida, M., Ii, S., Kitamura, K., Furukawa, T., Chiba, A., Hara, T., Hiraga, K., 1998. New deformation twinning mode of B19' martensite in Ti-Ni shape memory alloy. *Scr. Mater.* 39, 1749–1754.
- Nishida, M., Matsuda, M., Yasumoto, Y., Yano, S., Yamabe-Mitarai, Y., Hara, T., 2008b. Crystallography and morphology of twins in equiatomic TiPt martensite. *Mater. Sci. Technol.* 24, 884–889.
- Nishida, M., Ohgi, H., Itai, I., Chiba, A., Yamauchi, K., 1995a. Electron microscopy studies of twin morphologies in B19' martensite in the Ti-Ni shape memory alloy. *Acta Metallurgica et Materialia* 43, 1219–1227.
- Nishida, M., Yamauchi, K., Itai, I., Ohgi, H., Chiba, A., 1995b. High resolution electron microscopy studies of twin boundary structures in B19' martensite in the Ti-Ni shape memory alloy. *Acta Metallurgica et Materialia* 43, 1229–1234.
- Norfleet, D.M., Sarosi, P.M., Manchiraju, S., Wagner, M.F.X., Uchic, M.D., Anderson, P.M., Mills, M.J., 2009. Transformation-induced plasticity during pseudoelastic deformation in Ni-Ti microcrystals. *Acta Mater.* 57, 3549–3561.
- Ohba, T., Emura, Y., Miyazaki, S., Otsuka, K., 1990. Crystal Structure of  $\epsilon$  and  $\gamma$ ; Martensite in Au-47.5 at% Cd Alloy. *Mater. Trans.* 12–17. JIM 31.
- Okamoto, K., Ichinose, S., Morii, K., Otsuka, K., Shimizu, K., 1986. Crystallography of  $\beta 1 \rightarrow \gamma 1$  stress-induced martensitic transformation in a Cu-Al-Ni alloy. *Acta Metallurgica* 34, 2065–2073.
- Pond, R.C., Hirth, J.P., 2018. Topological model of type II deformation twinning. *Acta Mater.* 151, 229–242.
- Pond, R.C., Hirth, J.P., Knowles, K.M., 2019. Topological model of type II deformation twinning in NiTi martensite. *Philos. Mag.* 99, 1619–1632.
- Qian, X., Kawai, M., Goto, H., Li, J., 2015. Effect of twin boundaries and structural polytypes on electron transport in GaAs. *Comput. Mater. Sci.* 108, 258–263.
- Ren, G., Sehitoglu, H., 2016. Interatomic potential for the NiTi alloy and its application. *Comput. Mater. Sci.* 123, 19–25.
- Rooney, A.P., Li, Z., Zhao, W., Gholinia, A., Kozikov, A., Auton, G., Ding, F., Gorbachev, R.V., Young, R.J., Haigh, S.J., 2018. Anomalous twin boundaries in two dimensional materials. *Nat. Commun.* 9, 3597.
- Rothmann, M.U., Li, W., Zhu, Y., Bach, U., Spiccia, L., Etheridge, J., Cheng, Y.-B., 2017. Direct observation of intrinsic twin domains in tetragonal CH<sub>3</sub>NH<sub>3</sub>PbI<sub>3</sub>. *Nat. Commun.* 8, 14547.
- Sehitoglu, H., Karaman, I., Anderson, R., Zhang, X., Gall, K., Maier, H.J., Chumlyakov, Y., 2000. Compressive response of NiTi single crystals. *Acta Mater.* 48, 3311–3326.
- Shilo, D., Faran, E., Karki, B., Müllner, P., 2021. Twin boundary structure and mobility. *Acta Mater.* 220, 117316.
- Sidharth, R., Mohammed, A.S.K., Abuzaid, W., Sehitoglu, H., 2021. Unraveling frequency effects in shape memory alloys: NiTi and FeMnAlNi. *Shape Memory Superelastic.* 7, 235–249.
- Simon, T., Kröger, A., Somsen, C., Dlouhy, A., Eggeler, G., 2010. On the multiplication of dislocations during martensitic transformations in NiTi shape memory alloys. *Acta Mater.* 58, 1850–1860.
- Šittner, P., Molnárová, O., Kádárček, L., Tyc, O., Heller, L., 2020. Deformation twinning in martensite affecting functional behavior of NiTi shape memory alloys. *Materialia* 9, 100506.
- Wang, J., Xu, H., Gao, H., McDowell, D.L., 2024. Multiscale modeling of crystal defects in structural materials. *MRS Bull.* 49, 224–235.
- Wang, J., Zeng, Z., Weinberger, C.R., Zhang, Z., Zhu, T., Mao, S.X., 2015. In situ atomic-scale observation of twinning-dominated deformation in nanoscale body-centred cubic tungsten. *Nat. Mater.* 14, 594–600.
- Xie, Z.L., Liu, Y., 2004. HRTEM study of {011} type II twin in NiTi shape memory alloy. *Philos. Mag.* 84, 3497–3507.
- Xu, M., Chen, K., Cao, F., Velasco, L., Kaufman, T.M., Ye, F., Hahn, H., Han, J., Srolovitz, D.J., Pan, X., 2022. Disconnection-mediated Twin/Twin-junction migration in FCC metals. *Acta Mater.* 240, 118339.
- Ye, Y.Y., Chan, C.T., Ho, K.M., 1997. Structural and electronic properties of the martensitic alloys TiNi, TiPd, and TiPt. *Phys. Rev. B* 56, 3678–3689.
- Zárubová, N., Gemperlová, J., Gemperle, A., Dlabáček, Z., Šittner, P., Novák, V., 2010. In situ TEM observation of stress-induced martensitic transformations and twinning processes in CuAlNi single crystals. *Acta Mater.* 58, 5109–5119.
- Zhang, J., Somsen, C., Simon, T., Ding, X., Hou, S., Ren, S., Ren, X., Eggeler, G., Otsuka, K., Sun, J., 2012. Leaf-like dislocation substructures and the decrease of martensitic start temperatures: a new explanation for functional fatigue during thermally induced martensitic transformations in coarse-grained Ni-rich Ti–Ni shape memory alloys. *Acta Mater.* 60, 1999–2006.
- Zhang, Z., Sheng, H., Wang, Z., Gludovatz, B., Zhang, Z., George, E.P., Yu, Q., Mao, S.X., Ritchie, R.O., 2017. Dislocation mechanisms and 3D twin architectures generate exceptional strength-ductility-toughness combination in CrCoNi medium-entropy alloy. *Nat. Commun.* 8, 14390.
- Zhao, S., Zhang, R., Yu, Q., Ell, J., Ritchie, Robert, O., Minor Andrew, M., 2021. Cryoforged nanotwinned titanium with ultrahigh strength and ductility. *Science* 373, 1363–1368.
- Zhong, Y., Gall, K., Zhu, T., 2011. Atomistic study of nanotwins in NiTi shape memory alloys. *J. Appl. Phys.* 110, 033532.
- Zhu, Q., Huang, Q., Tian, Y., Zhao, S., Chen, Y., Cao, G., Song, K., Zhou, Y., Yang, W., Zhang, Z., An, X., Zhou, H., Wang, J., 2022. Hierarchical twinning governed by defective twin boundary in metallic materials. *8*, eabn8299.
- Zou, N., Li, Z., Zhang, Y., Yang, B., Zhao, X., Esling, C., Zuo, L., 2018. Plastic deformation of Ni–Mn–Ga 7M modulated martensite by twinning & detwinning and intermartensitic transformation. *Int. J. Plastic.* 100, 1–13.